J. Fluid Mech. (1987), *vol.* 176, *pp.* 191–219
Printed in Great Britain

The evolution of instabilities in the axisymmetric jet. Part 1. The linear growth of disturbances near the nozzle

By J. COHEN† AND I. WYGNANSKI‡
Aerospace and Mechanical Engineering Department, University of Arizona, Tucson, AZ 85721, USA

(Received 11 February 1986)

The modal distributions of coherent structures evolving near the nozzle of a circular jet are considered. The effects produced on the instability modes by transverse curvature, flow divergence, inhomogeneous inflow conditions, and the detailed shape of the mean velocity profile, are investigated both theoretically and experimentally. Linear stability analysis applied to a thin shear layer surrounding a large-diameter jet (i.e. a jet whose diameter is large in comparison with a typical width of the shear layer) indicates that many azimuthal modes are equally unstable. An increase in the relative thickness of the shear layer limits the number of unstable modes, and only one helical mode remains unstable at the end of the potential core. The linear model used as a transfer function is capable of predicting the spectral distribution of the velocity perturbations in a jet. This provides a rational explanation for the stepwise behaviour of the predominant frequency resulting from a continuous increase in the jet velocity.

1. Introduction

The initial evolution of an axisymmetric jet has been carefully and continuously investigated ever since jet propulsion became technologically feasible. Nevertheless, the mechanisms affecting mixing, combustion and the generation of noise are not completely understood nor can they be fully predicted or controlled.

It was initially believed that the statistically describable behaviour of a turbulent jet is totally independent of the conditions near the nozzle. The discovery of large coherent structures (Crow & Champagne 1971; Brown & Roshko 1971) in the mixing layer and in the developing portion of the axisymmetric jet started a new trend of investigations attempting to assess the connection between these structures and the evolution of the flow. The large coherent structures whose characteristic dimensions are commensurate with the width of the flow resemble the vortices generated by an inviscid instability.

The roll-up of travelling instability waves into a periodic array of vortices in a plane mixing layer was predicted by Michalke (1965) and demonstrated experimentally by Freymuth (1966). The analysis was extended by Michalke (1971) and his coworkers to include the effects of compressibility, circular geometry, variations in the shape of the velocity profile, and disturbances propagating in the spanwise direction. The

† Present address: Department of Aeronautics and Astronautics, Massachusetts Institute of Technology, Cambridge, MA 02139, USA.
‡ Also School of Engineering, Tel Aviv University, Tel Aviv, Israel.

application of the analysis to a non-divergent shear layer is rather restrictive because it implies that at some distance downstream *only* the most amplified wave will dominate the flow. In practice, however, the width of the shear layer increases in the direction of streaming, resulting in a continuous shift of the most amplified instability waves toward lower and lower frequencies. This effect was realized by Mattingly & Chang (1974), who tried to adapt the quasi-parallel stability calculations to their axisymmetric-jet experiment. Crighton & Gaster (1976) used a multiple-scale expansion, in terms of a small parameter defining the divergence of the mean flow, to calculate the growth rates and phase speeds of large-scale, but small-amplitude, wavy disturbances in an axisymmetric jet. This expansion method was applied by Gaster, Kit & Wygnanski (1985) to a divergent plane mixing layer and compared with an experiment conducted in a fully turbulent flow. The applicability of the linear stability theory to turbulent flow is somewhat questionable because there is no steady velocity field in existence upon which a small perturbation may be superimposed. One tends to select the mean velocity profile as being the representative quantity of the steady motion, recognizing the possibility that such a profile might never occur at any instant in time. By assuming that the random changes in the mean velocity occur on a timescale that is short in comparison with a representative period associated with the large coherent structures and by neglecting possible exchanges of momentum among largely disparate scales, Gaster *et al.* applied the inviscid stability theory with a large measure of success. This gave an impetus to the present investigation, whose initial purpose was limited to the application of the linear model to the axisymmetric jet.

The thin axisymmetric shear layer is unstable to a large number of discrete azimuthal modes (Plaschko 1979), but the fully developed jet, at some distance beyond the termination of the potential core, is unstable to the helical mode only (Batchelor & Gill 1962). The first comprehensive study of the response of an axisymmetric jet to a controlled axisymmetric (mode $m = 0$) excitation was done by Crow & Champagne (1971). They observed the emergence of large wave-like structures which attained the greatest total downstream amplification at a Strouhal number, based on the jet diameter, of 0.3; wave modes of higher frequencies peaked closer to the nozzle exit while those of lower frequencies persisted farther downstream. The excitation also affected the mean flow near the nozzle and, although the level of the excitation is considered to be high, the structures observed resemble wave-like structures photographed earlier in the turbulent flow of a high-Reynolds-number, unexcited jet (Bradshaw, Ferris & Johnson 1964). Michalke (1971), Fuchs (1972) and Mattingly & Chang (1974) all recognized the potential importance of the helical ($m = 1$) mode which should have been amplified in an axisymmetric jet at rates that are comparable, at least, to the amplification rates of the plane ($m = 0$) mode of instability. Experimental evidence for the existence of spinning modes in a high-Reynolds-number jet was sketchy. Drubka (1981) observed these instabilities visually in the jet core region. Flow visualization based on laser-induced fluorescence in a fully developed axisymmetric jet suggests that the spinning mode dominates the flow at large distances from the nozzle exit (Dimotakis, Lye & Papantoniou 1983).

The experiments reported by Strange (1981) represent a systematic study in which an axisymmetric, high-Reynolds-number jet was excited at three modes ($m = 0$, 1 and 2) independently. The measurements are compared with the linear stability analysis (Plaschko 1979; Strange & Crighton 1983) and show that the growth rates of modes $m = 0$ and 1 are comparable. The phase velocities and the radial distribution of the educed large structures compare quite well with the theory, but the streamwise

rates of amplification do not. The unfavourable comparison with measured data appears to stem, in part, from the nonlinear response of the instability to the strong levels of excitation used, but the type and form of the predominant nonlinear interactions cannot easily be determined from Strange's data.

The overall purpose of this research is to examine the generation of large coherent structures in a jet, assuming that they are synonymous with instability modes, and to observe their evolution in the direction of streaming in the presence of the leading nonlinearities. In the first part of this investigation, some of the peculiarities of the axisymmetric configuration and the inhomogeneous conditions existing in the plane of the nozzle are discussed. For example, the effects of the transverse curvature on the evolution of disturbances in the mixing layer surrounding the core of the jet are analysed. These effects are often neglected on the premise that the shear layer is thin relative to the radius of curvature of the core, but this premise is violated a short distance downstream of the nozzle. The finite dimension of the core may limit the number of unstable modes able to coexist and interact at any given cross-section.

2. A description of the apparatus and methods of data acquisition

2.1. *The jet facility and the instrumentation*

A schematic diagram of the jet facility is shown in figure 1. The air used in the experiment is supplied by a central, high-pressure source (100 p.s.i.g.). The air passes through pressure regulators and control valves before entering the apparatus at the top of a rectangular plenum chamber. It then passes through a series of perforated plates and acoustic dampeners before entering a smaller cylindrical plenum. This chamber is approximately 80 cm long and has a circular cross-section 30 cm in diameter; it houses two automobile air filters, a honeycomb, and three screens. The flow exits through a spun aluminium nozzle ending with a diameter of 5 cm. At the end of the nozzle, the flow attains a 'top-hat' velocity profile, with the exception of a thin boundary layer present near the solid surface.

A unique traversing mechanism (figure 2), controlling the axial and radial movement of the hot-wire probes used for measurement of velocity, was designed. It positions eight hot-wire sensors (displaced azimuthally 45° apart) *individually* at any prescribed radial location; it is then capable of moving all sensors simultaneously an equal distance in the radial direction. A speaker was placed at the base of the plenum chamber to generate controlled, axisymmetric disturbances at the exit plane of the nozzle. Eight speakers, equally displaced around the azimuth, generated higher-order modes by blowing thin jets of air through narrow slits located near the lip of the nozzle. These speakers were driven by a phase-shifting network which was activated at the desired frequencies and amplitudes by a signal coming from a function generator and passing through a power amplifier. The jet velocity U_j varied between 3 m/s and 8.5 m/s, changing the Reynolds number based on the exit diameter of the nozzle from 10^4 to 2.9×10^4, while the turbulence level at the exit plane of the jet changed from 0.17 % at 3 m/s to 0.094 % at 8 m/s.

Hot-wire anemometers, which were built locally, were used in conjunction with Disa Model 55P11 sensors throughout this investigation. The hot wires, made of tungsten, were 5 μm in diameter and had a length-to-diameter ratio of 300; they were kept at a constant overheat ratio of 1.8 and had a maximum frequency response of 30 KHz. The signals were amplified to take advantage of the maximum dynamic range of the analog-to-digital converter, which operated between ± 10 V. All channels

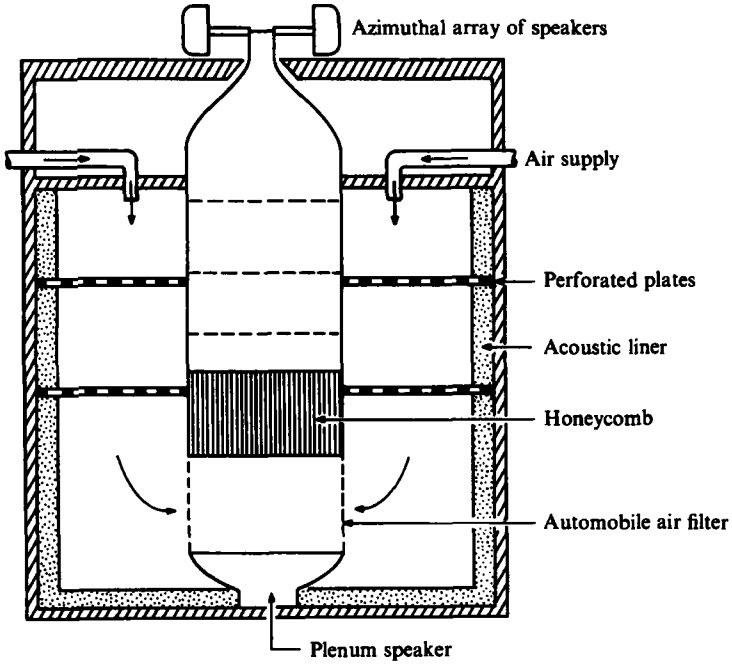

FIGURE 1. Air-jet facility.

were sampled simultaneously 4096 times a second, giving a maximum frequency response (Nyquist frequency) of 2048 Hz.

In order to retain phase information, the excitation signal was recorded together with the velocity information. The sampling frequency was 36 times higher than the frequency of the excited wave, giving a cyclical resolution of 2° relative to the fundamental component of the phase-locked signal. The typical length of a velocity record used for averaging was equivalent to 480 periods of the excitation frequency. The data were stored on a digital tape. The computer used for data acquisition was the DEC LSI 1123.

The hot wires were calibrated in the exit plane of the jet against a standard Pitot tube at seven different velocities. Before the initiation of data acquisition, the radial location of each of the eight wires was adjusted relative to mean flow, rather than by geometry. This was done by placing each of the eight hot wires at the centre of the mixing layer ($r = R_{\frac{1}{2}}$), where the mean velocity is reduced to one-half of the centreline value. After completing the fine alignment of the probes, the flow was traversed by all wires simultaneously in the radial direction. The location $R_{\frac{1}{2}}$ for each mean velocity profile was determined by using a least-squares fit to all data points at which the mean velocities satisfied $0.35 \leqslant U/U_j \leqslant 0.65$.

2.2. *The decomposition of phase-locked data into azimuthal modes*

Let $q(t, \phi)$ represent a signal having a periodicity T in the time (t) domain and 2π in the azimuthal coordinate (ϕ). For a constant ϕ (ϕ may also be considered as a parameter), the signal can be expressed as a Fourier series

$$q(t,\phi) = a_0(\phi) + \sum_{n=1}^{\infty} [a_n(\phi)\cos(n\beta t) + b_n(\phi)\sin(n\beta t)], \tag{2.1a}$$

(*a*)

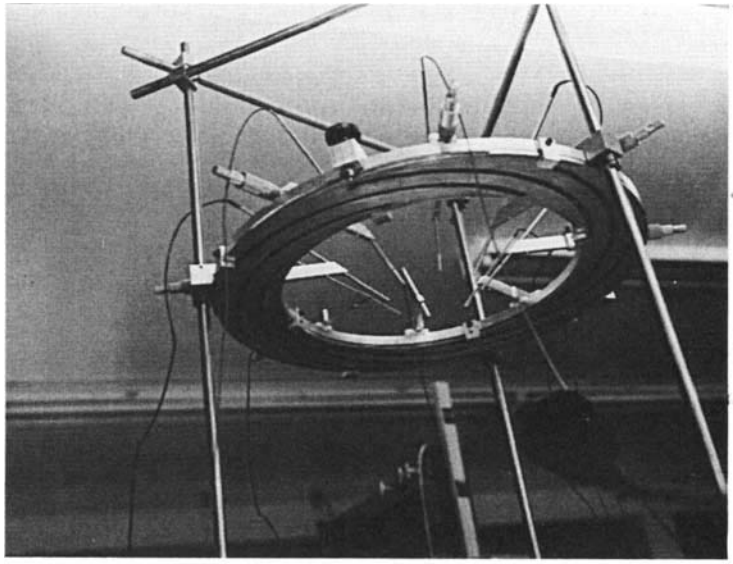

(*b*)

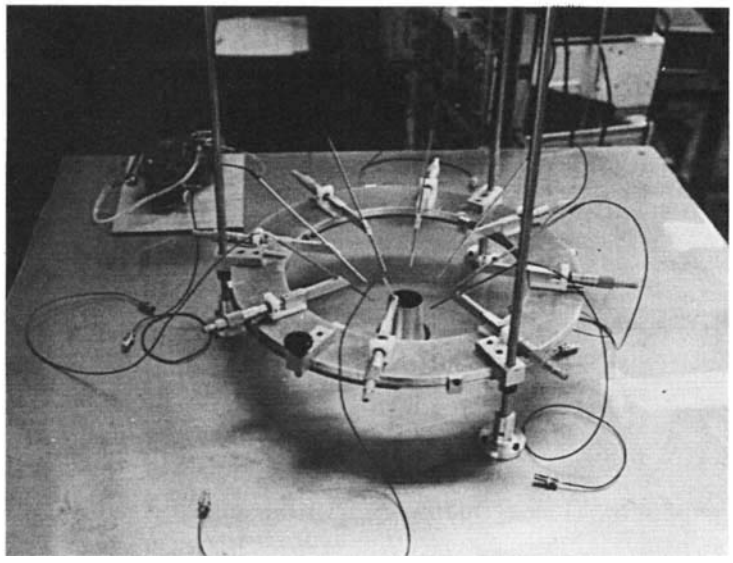

FIGURE 2. Radial traverse: (*a*) bottom view showing spiral grooves; (*b*) top view showing jet nozzle.

where β is the fundamental frequency, n is a positive integer, and the coefficients a_n and b_n are determined by the orthogonality condition

$$a_0(\phi) = \frac{1}{T}\int_0^T q(t,\phi)\,\mathrm{d}t; \quad \begin{pmatrix} a_n(\phi) \\ b_n(\phi) \end{pmatrix} = \frac{2}{T}\int_0^T q(t,\phi)\begin{bmatrix} \cos(n\beta t) \\ \sin(n\beta t) \end{bmatrix}\mathrm{d}t. \tag{2.1b}$$

The fundamental component (q_f) of the signal is determined by considering the fundamental periodicity only (i.e. by letting $n = 1$),

$$q_f(\tau,\phi) = a_f(\phi)\cos(2\pi\tau) + b_f(\phi)\sin(2\pi\tau), \tag{2.2a}$$

with

$$\begin{pmatrix} a_f(\phi) \\ b_f(\phi) \end{pmatrix} = 2\int_0^1 q(\tau,\phi)\begin{bmatrix}\cos(2\pi\tau)\\ \sin(2\pi\tau)\end{bmatrix}\mathrm{d}\tau, \tag{2.2b}$$

where τ is the dimensionless time expressed as a fraction of the period T (i.e. $\tau = t/T$). Using the periodicity 2π in the azimuthal direction, the coefficients $a_f(\phi)$ and $b_f(\phi)$ can be expressed as

$$a_f(\phi) = c_0 + \sum_{m-1}^{\infty}[c_m\cos(m\phi) + d_m\sin(m\phi)], \tag{2.3a}$$

where

$$c_0 = \frac{1}{2\pi}\int_0^{2\pi} a_f(\phi)\,\mathrm{d}\phi; \quad \begin{pmatrix} c_m \\ d_m \end{pmatrix} = \frac{1}{\pi}\int_0^{2\pi} a_f(\phi)\begin{bmatrix}\cos(m\phi)\\ \sin(m\phi)\end{bmatrix}\mathrm{d}\phi, \tag{2.3b}$$

and similarly

$$b_f(\phi) = e_0 + \sum_{m-1}^{\infty}[e_m\cos(m\phi) + g_m\sin(m\phi)], \tag{2.4a}$$

where

$$e_0 = \frac{1}{2\pi}\int_0^{2\pi} b_f(\phi)\,\mathrm{d}\phi; \quad \begin{pmatrix} e_m \\ g_m \end{pmatrix} = \frac{1}{\pi}\int_0^{2\pi} b_f(\phi)\begin{bmatrix}\cos(m\phi)\\ \sin(m\phi)\end{bmatrix}\mathrm{d}\phi. \tag{2.4b}$$

Substituting (2.3) and (2.4a) into (2.2a), one obtains

$$q_f(\tau,\phi) = \left[c_0 + \sum_{m-1}^{\infty}\{c_m\cos(m\phi) + d_m\sin(m\phi)\}\right]\cos(2\pi\tau) + \left[e_0 + \sum_{m-1}^{\infty}\{e_m\cos(m\phi) + g_m\sin(m\phi)\}\right]\sin(2\pi\tau). \tag{2.5}$$

Equation (2.5) represents a pattern in which the amplitude of the wave (the term inside the square brackets) varies sinusoidally with ϕ while the temporal periodicity is independent of the azimuthal coordinate.

For the axisymmetric case ($m = 0$), one obtains

$$q_{f,0}(\tau) = A_0\cos(2\pi\tau + \gamma_0); \quad A_0 = (c_0^2 + e_0^2)^{\frac{1}{2}}; \quad \gamma_0 = \tan^{-1}\frac{e_0}{c_0}, \tag{2.6}$$

where A_0 is the amplitude of the wave and γ_0 is its phase. For higher-order modes ($m \neq 0$),

$$q_{f,m}(\tau,\phi) = [c_m\cos(m\phi) + d_m\sin(m\phi)]\cos(2\pi\tau) + [e_m\cos(m\phi) + g_m\sin(m\phi)]\sin(2\pi\tau). \tag{2.7}$$

In order to express (2.7) as a combination of running waves, the following substitutions are made:

$$\left.\begin{aligned} l &= \tfrac{1}{2}(c_m + g_m); \quad j = \tfrac{1}{2}(d_m + e_m);\\ h &= \tfrac{1}{2}(c_m - g_m); \quad k = \tfrac{1}{2}(e_m - d_m).\end{aligned}\right\} \tag{2.8}$$

Then, after using simple trigonometric relations, (2.7) has the form

$$q_{f,m} = A_{+m}\cos(2\pi\tau - m\phi - \gamma_{+m}) + A_{-m}\cos(2\pi\tau + m\phi - \gamma_{-m}), \tag{2.9a}$$

where

$$\left.\begin{aligned} A_{+m} &= (l^2 + k^2)^{\frac{1}{2}}; \quad A_{-m} = (h^2 + j^2)^{\frac{1}{2}};\\ \gamma_{+m} &= \tan^{-1}\left(\frac{k}{l}\right); \quad \gamma_{-m} = \tan^{-1}\left(\frac{j}{h}\right).\end{aligned}\right\} \tag{2.9b}$$

A_{+m} and γ_{+m} represent the amplitude and the phase, respectively, of a forward-running wave while A_{-m} and γ_{-m} represent the amplitude and phase of a backward-running wave.

3. Analysis

3.1. *Some unique features of the axisymmetric configuration*

3.1.1. *Dimensional considerations*

A single velocity scale and a single lengthscale may describe the evolution of a plane wavetrain in a two-dimensional mixing layer. A quotient between the wavelength of the disturbance, which has a characteristic frequency F_f and is convected downstream at a velocity U_c ($\lambda_x = U_c/F_f$), and a typical width of the mixing layer θ yields a dimensionless number $2\pi F_f \theta/U_c$ which controls the amplification or the decay of the perturbation. The mean flow in the axisymmetric mixing layer is constricted by the diameter of the jet column, which introduces an additional lengthscale into this problem, permitting the evolution of an infinite number of discrete helical instability modes.

To explore the importance of the additional length ($R_{\frac{1}{2}}$) relative to an azimuthal wavelength with which it may scale, the following dimensional analysis was carried out. The velocity and pressure fluctuations used in the stability analysis are described by

$$u = F_u(r) \exp[\mathrm{i}(\alpha x - \beta t + m\phi)] + (*), \tag{3.1a}$$

$$v = F_v(r) \exp[\mathrm{i}(\alpha x - \beta t + m\phi)] + (*), \tag{3.1b}$$

$$w = F_w(r) \exp[\mathrm{i}(\alpha x - \beta t + m\phi)] + (*), \tag{3.1c}$$

$$p = F_p(r) \exp[\mathrm{i}(\alpha x - \beta t + m\phi)] + (*), \tag{3.1d}$$

where $F_u(r)$, $F_v(r)$ and $F_w(r)$ are the amplitudes of the three components of the velocity perturbation in the streamwise direction (x), the radial direction (r), and the azimuthal direction (ϕ), respectively; $F_p(r)$ represents the pressure fluctuation; the symbol (*) refers to a complex-conjugate term; β is the frequency of the wave ($\beta = 2\pi F_f$); m is the azimuthal mode number; and α is a complex constant whose real part (α_r) gives the wavenumber while the imaginary part (α_i) describes the growth rate of the wave.

The linear disturbance equation, expressed in terms of the amplitude of the pressure fluctuation F_p (Plaschko 1979) for inviscid and incompressible flow, is given by

$$\frac{\mathrm{d}^2 F_p}{\mathrm{d}r^2} + \left[\frac{1}{r} - \frac{2\,\mathrm{d}\overline{U}_0/\mathrm{d}r}{\overline{U}_0 - c}\right] \frac{\mathrm{d}F_p}{\mathrm{d}r} - \left[\frac{m^2}{r^2} + \alpha^2\right] F_p = 0, \tag{3.2}$$

where $\overline{U}_0(r)$ is the prescribed mean velocity profile and $c = \beta/\alpha$, for which the ratio β/α_r represents the phase velocity of the wave c_{ph}.

Shifting the origin of the coordinate system to the centre of the shear layer by letting the width of the jet column $R_{\frac{1}{2}}$ coincide with the radial distance at which the local mean velocity drops to one-half of its value on the centreline $U_{\mathbb{C}}$ and dividing each length by an equivalent plane momentum thickness of the shear layer

$$\theta = \int_0^\infty \frac{\overline{U}_0}{U_{\mathbb{C}}} \left(1 - \frac{\overline{U}_0}{U_{\mathbb{C}}}\right) \mathrm{d}r,$$

and each velocity by $U_{\mathbb{C}}$ defines the following dimensionless quantities:

$$\left.\begin{aligned} \tilde{U}_0 &= \frac{\overline{U}_0}{U_{\mathbb{C}}}; \quad \tilde{y} = \frac{r-R_{\frac{1}{2}}}{\theta}; \quad \tilde{\alpha} = \alpha\theta; \\ \tilde{\beta} &= \frac{\beta\theta}{U_{\mathbb{C}}}; \quad \tilde{F}_p = \frac{F_p}{\rho U_{\mathbb{C}}^2}; \quad \tilde{c} = \frac{c}{U_{\mathbb{C}}} = \frac{\tilde{\beta}}{\tilde{\alpha}} \end{aligned}\right\} \tag{3.3}$$

The dimensionless form of (3.2) becomes

$$\tilde{F}_p'' + \left[\frac{1}{\tilde{y}+\left(\frac{R_{\frac{1}{2}}}{\theta}\right)} - \frac{2\tilde{U}_0'}{\tilde{U}_0-\tilde{c}}\right]\tilde{F}_p' - \left[\frac{m^2}{\left(y+\frac{R_{\frac{1}{2}}}{\theta}\right)^2} + \tilde{\alpha}^2\right]\tilde{F}_p = 0, \tag{3.4}$$

where differentiation with respect to $\tilde{y}$ is denoted by a prime.

Equation (3.4) reflects the importance of the parameter $R_{\frac{1}{2}}/\theta$, describing the ratio between the radius of the jet and the width of the shear layer. The significance of this parameter is appreciated by recalling that, in the two-dimensional mixing layer, a given ratio of θ/λ determines uniquely the solution for an amplified mode. In the axisymmetric case, a whole family of solutions depending on the parameter $R_{\frac{1}{2}}/\theta$ exists (see also Michalke & Hermann 1982). Moreover, by substituting the azimuthal wavelength ($\lambda_\phi = 2\pi R_{\frac{1}{2}}/m$) into the last term in (3.4) (as will be demonstrated in §3.2.1), the importance of the ratio between the azimuthal and axial wavelengths becomes apparent.

3.1.2. *The natural evolution of disturbances in the axisymmetric mixing layer*

The length of the potential core, determined from the constancy of the velocity on the centreline of the jet, is approximately 3.5 diameters for $Re_D = U_j D/\nu \approx 2.7\times10^4 (U_j = 8$ m/s), as shown in figure 3. The mixing layer is almost parallel near the nozzle ($x/D \leqslant 0.5$) but it spreads rapidly farther downstream ($1 \leqslant x/D \leqslant 4$). Nevertheless, the ratio $R_{\frac{1}{2}}/\theta$ decreases steeply from $x/D = 0.125$ (figure 3). Mean velocity profiles normalized by the local velocity of the jet on the centreline ($U_{\mathbb{C}}$) are plotted versus $(r-R_{\frac{1}{2}})/\theta$ for several downstream locations in figure 4. The solid lines describe a family of fitted profiles having the form

$$\left.\begin{aligned} \overline{U}_0(\eta) &= 0.5\{1-\tanh\eta\,[1+\operatorname{sech}^2\eta\,(C_1\tanh\eta + C_2)]\}; \\ \eta &= 0.5\,C_3\,\frac{r-R_{\frac{1}{2}}}{\theta}, \end{aligned}\right\} \tag{3.5}$$

where $\overline{U}_0(\eta) = U/U_{\mathbb{C}}$; C_1 and C_2 are constants describing the symmetric and antisymmetric corrections, respectively, to the classical hyperbolic tangent profile; and C_3 represents the divergence of the centre of the mixing layer from the centreline of the jet. The last constant is related to C_1 and C_2 by the definition of the quasi-two-dimensional momentum thickness and is given by

$$C_3 = 1 - \tfrac{2}{3}C_2 - \tfrac{2}{35}C_1^2 - \tfrac{2}{15}C_2^2. \tag{3.6}$$

This equation applies whenever a potential core having a constant velocity $U_{\mathbb{C}}$ exists. The velocity profiles shown in figure 4 are not self-similar since θ does not increase linearly with x (figure 3). One may recall that the velocity profiles chosen by Michalke (1971) were also not self-similar.

Linear stability analysis was applied to this family of the mean velocity profiles for the first seven azimuthal modes after assuming that the flow is inviscid and

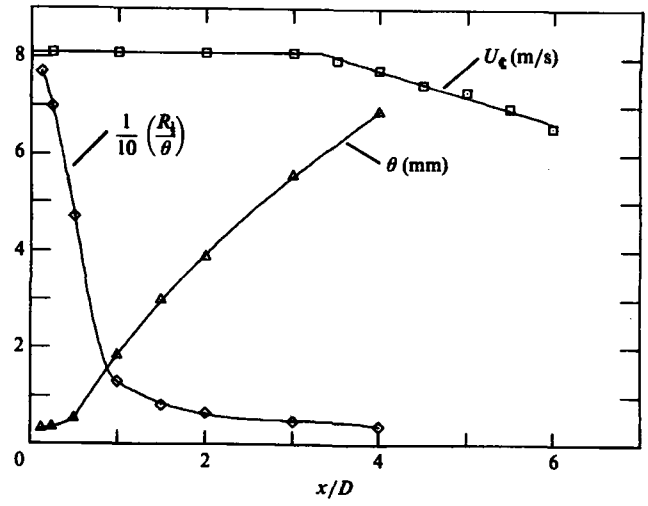

FIGURE 3. Streamwise variation of length and velocity scales: △, planar momentum thickness; ◇, ratio between jet radius and the planar momentum thickness; □, centreline mean velocity.

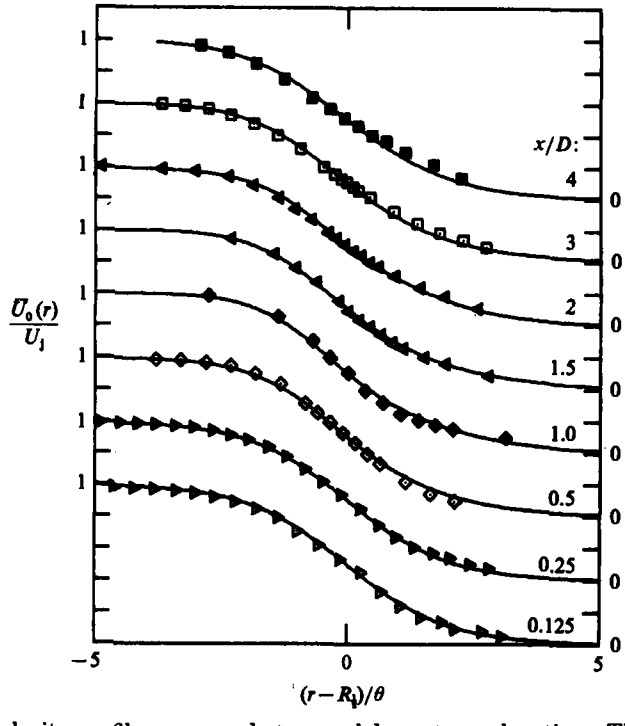

FIGURE 4. Mean velocity profiles measured at several downstream locations. The symbols represent data points and the solid lines represent fitted profiles having the form given in equation (3.5).

quasi-parallel ($0 \leqslant m \leqslant 6$). The dimensionless amplification rates $-\alpha_i\theta$ were calculated as a function of the dimensionless frequency $2\pi f\theta/U_{\mathbb{C}}$ for all the streamwise locations. These calculations show that at $x/D = 0.125$ (corresponding to $R_j/\theta = 77$), the amplification rates of the first four azimuthal modes are almost indistinguishable from one another; only the maximum amplification rates of modes 4–6 fall slightly

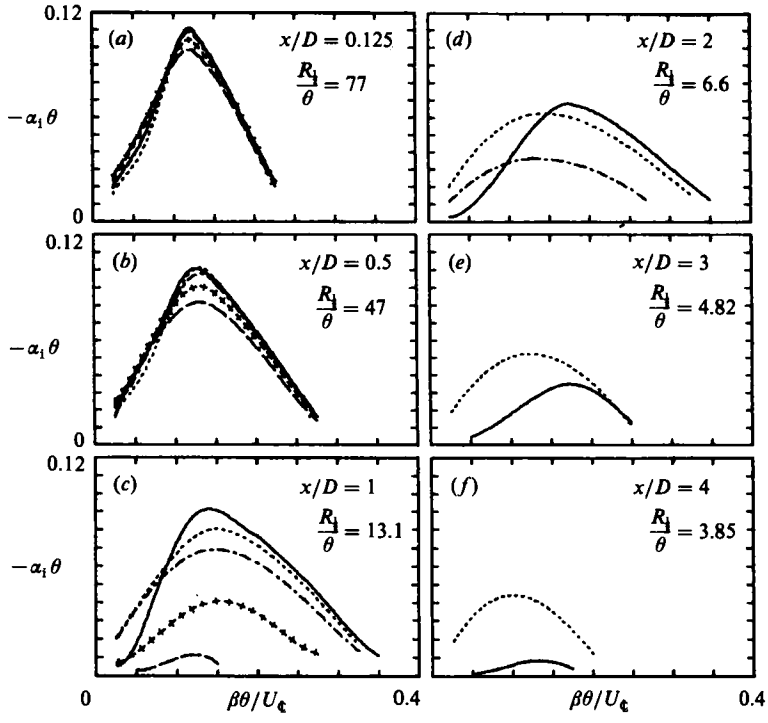

FIGURE 5. Spatial growth ratio $-\alpha_i\theta$ as a function of the dimensionless frequency $\beta\theta/U_{\mathbb{C}}$ as calculated for several downstream locations and mode numbers: ——, $m = 0$; – – –, 1, –·–·–, 2; + + +, 4; — — —, 6.

short of the maximum rates attained by the lower azimuthal modes (figure 5*a*). As the mixing layer widens ($R_{\frac{1}{2}}/\theta$ decreases), the relative importance of the higher azimuthal modes ($m \geqslant 2$) diminishes and, at the end of the potential core, only the helical ($m = 1$) and the axisymmetric ($m = 0$) modes remain amplified (figure 5*f*). At large values of $R_{\frac{1}{2}}/\theta$ (corresponding to $x/D = 0.5$), there is no observable difference in the amplification rate of modes 0 and 1; at $R_{\frac{1}{2}}/\theta \approx 13.1$ (i.e. $x/D = 1$), the axisymmetric mode undergoes the strongest amplification at all but the lowest frequencies. At $R_{\frac{1}{2}}/\theta = 6.6$ ($x/D = 2$), the strongest rate of amplification for both modes is almost equal; the axisymmetric mode dominates the disturbances at high frequencies while the helical mode does so in the low-frequency range of the spectrum. At $R_{\frac{1}{2}}/\theta \leqslant 4.82$ ($x/D \geqslant 3$), the amplification rate of the helical mode dominates the flow at all frequencies; consequently, one expects this mode to control the evolution of the fully developed axisymmetric wakes and jets (see Batchelor & Gill 1962; Mattingly & Chang 1974).

The emergence of mode 1 as the dominant instability at the end of the potential core was also predicted by Michalke & Hermann (1982). Their quantitative results are, however quite different. In order to assess the source of these differences the stability calculations were repeated for the velocity profile used by Michalke & Hermann, reproducing their results identically. A detailed comparison between the two sets of calculations is provided in figure 6 for $R_{\frac{1}{2}}/\theta = 13.1$ and 3.85. The two velocity profiles are compared in figure 6(*a*, *b*). The solid curve fits the data obtained in the present experiments (equation 3.5) while the dotted profile corresponds to the one used by Michalke & Hermann. The calculated spatial amplification rates for modes 0 and 1 are shown in figure 6(*c*, *d*).

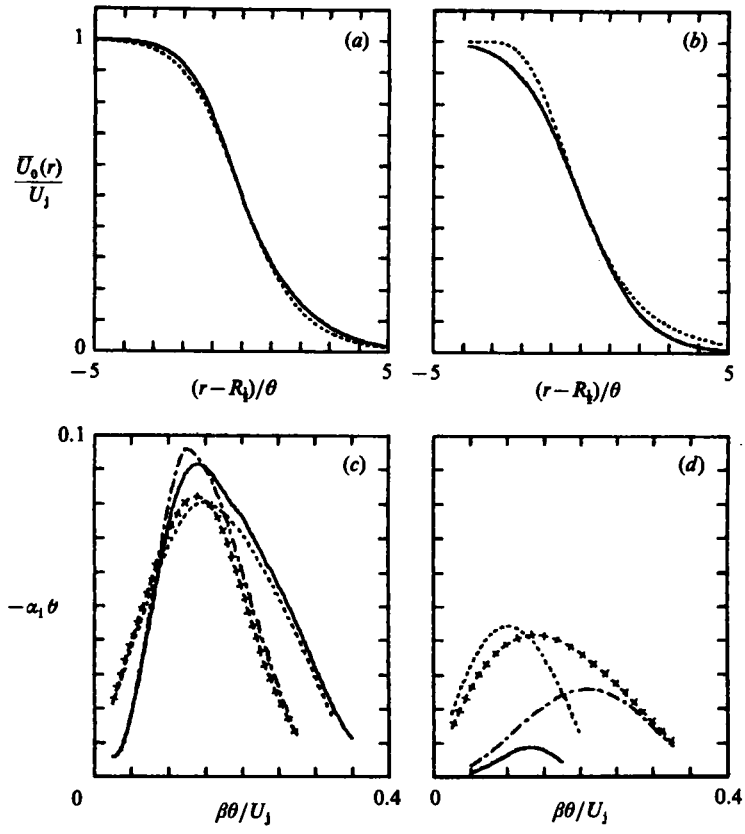

FIGURE 6. Comparison of the stability of calculations obtained in the present investigation with those obtained by Michalke & Hermann (1982). (*a*) mean velocity profiles for $R_{\frac{1}{2}}/\theta = 13.1$: ——, profiles used in the present investigation; – – –, profile used by Michalke & Hermann. (*b*) As (*a*) but for $R_{\frac{1}{2}}/\theta = 3.85$. (*c*) Spatial growth rate versus the dimensionless frequency as calculated for the mean profiles given in (*a*); based on the solid profile: ——, $m = 0$; – – –, $m = 1$; based on the broken profile: –·–·–, $m = 0$; + + +, $m = 1$. (*d*) As (*c*) but for $R_{\frac{1}{2}}/\theta = 3.85$.

The potential core terminates in the present calculations at $x/D = 4$ and $R_{\frac{1}{2}}/\theta = 3.85$, while it still prevails according to the mean profile chosen by Michalke & Hermann (1982) even at lower values of $R_{\frac{1}{2}}/\theta$. The diameter of the jet column, as expressed by the location at which $\tilde{y} = 0$, is therefore an additional independent length governing the instabilities.

One may conclude from this comparison that, for identical values of $R_{\frac{1}{2}}/\theta$, the radial velocity gradient affects the range of amplified frequencies as well as the number of the amplified modes. The calculations made in the present paper at $R_{\frac{1}{2}}/\theta = 3.85$ suggest that the amplification rate of the axisymmetric mode is insignificant relative to the helical mode for all frequencies considered. The calculations of Michalke & Hermann (1982), for identical $R_{\frac{1}{2}}/\theta$, indicate, on the other hand, that the amplification rates of modes 1 and 0 are identical for Strouhal number $St_\theta > 0.25$. The calculations presented in our work are in agreement with the conclusions of Batchelor & Gill (1962), who stated that the axisymmetric perturbations cannot amplify in the fully developed jet.

The variation of phase velocities with St_θ for various $R_{\frac{1}{2}}/\theta$ are plotted in figure 7. For large St_θ, corresponding to high-frequency oscillations, and for $R_{\frac{1}{2}}/\theta \geqslant 10$, all modes calculated are non-dispersive; the dispersiveness of the various modes spreads

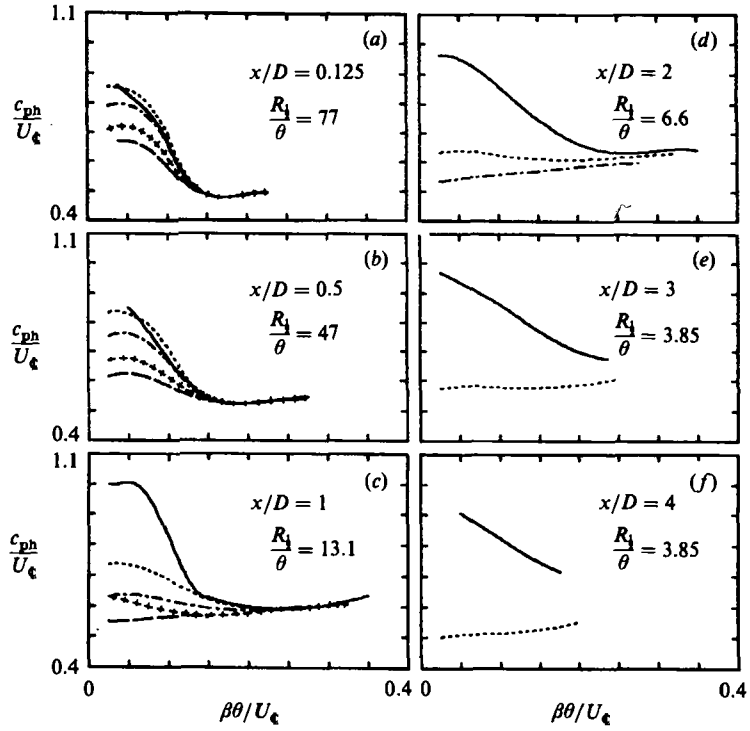

FIGURE 7. Phase velocity $c_{ph}/U_{\mathbb{C}}$ as a function of the dimensionless frequency $\beta\theta/U_{\mathbb{C}}$ as calculated for several downstream locations and mode numbers. ——, $m = 0$; – – –, 1; –·–·–, 2; + + +, 4; — — —, 6.

toward higher St_θ with decreasing R_δ/θ. At $R_\delta/\theta < 5$ (corresponding to $x/D > 3$), the axisymmetric mode is dispersive over the entire range of its amplified frequencies while the azimuthal mode is not dispersive at all. At $x/D = 3$, the normalized phase velocity of the zeroth mode varies from $0.65 < c_{ph}/U_{\mathbb{C}} < 1$ while the corresponding phase velocity of mode 1 is 0.57 irrespective of St_θ,. The phase velocity of this mode decreases slightly with increasing x/D, varying from 0.63 at $x/D = 2$ to 0.52 at $x/D = 4$. The large eddies in an axisymmetric mixing layer are convected downstream at a velocity in the range $0.65\,U_{\mathbb{C}}$ to $0.5\,U_{\mathbb{C}}$ between $2 \leqslant x/D \leqslant 4$ (Petersen 1978; Bradshaw *et al.* 1964; Davies, Fisher & Barratt 1963). It is suggested, therefore, that the azimuthal mode is prevalent at the end of the potential core. Flow visualization in an unexcited jet (Dimotakis *et al.* 1983) provides some additional evidence that this may be the case.

The fact that for $R_\delta/\theta > 10$ many modes are not dispersive over a broad range of frequencies permits resonant interactions to occur. The non-dispersive character among so many modes (at $R_\delta/\theta > 10$) over a broad range of frequencies makes a variety of resonant interactions possible; some of these interactions will be discussed in Part 2 of this paper (Cohen & Wygnanski 1987).

The dependence of the maximum amplification rates on the distance from the nozzle is plotted in figure 8(*a*) for several azimuthal modes, and the corresponding frequencies St_θ at which the maximum amplification rate occurs are plotted in figure 8(*b*). The distance over which a given mode amplifies become shorter with increasing mode number except for mode 0, whose amplification rate is overtaken by mode 1 at $x/D \approx 2.5$. The Strouhal number of the most amplified axisymmetric mode is

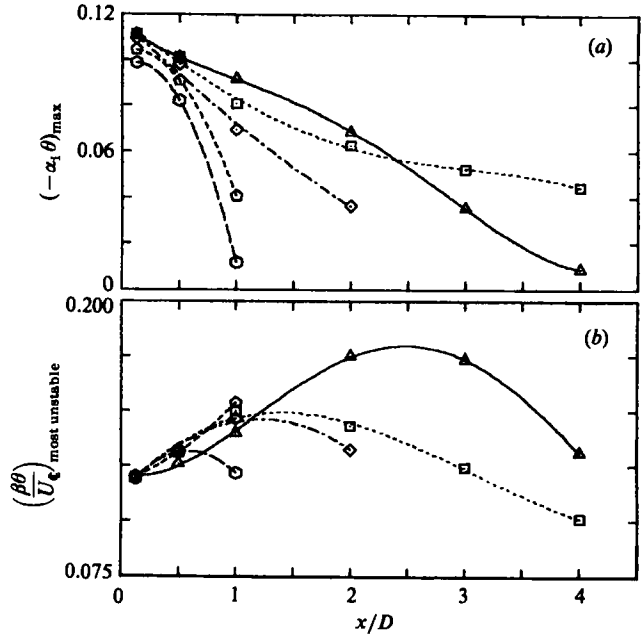

FIGURE 8. Streamwise variation of (*a*) the spatial growth rate of the most amplified wave, (*b*) the corresponding dimensionless frequency: ▲, $m = 0$; ⊡, 1; ◇, 2; ◇, 4; ⊙, 6.

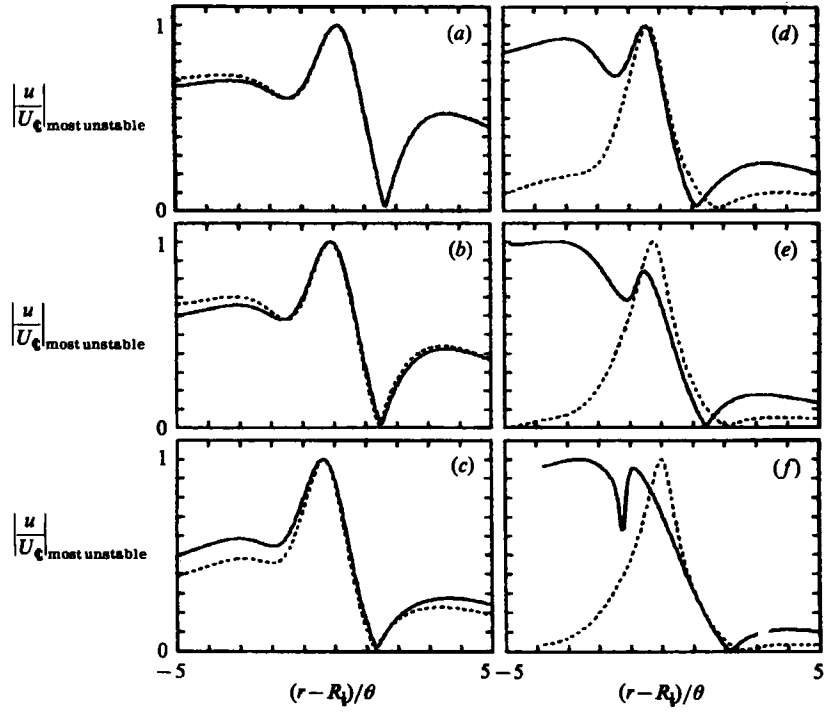

FIGURE 9. Radial distributions of the amplitudes of the streamwise velocity component of the oscillations as calculated for several downstream locations for modes: ——, $m = 0$; – – –, 1. (*a*) $x/D = 0.125$; (*b*) 0.5; (*c*) 1.0; (*d*) 2.0; (*e*) 3.0; (*f*) 4.0.

much larger than the corresponding St_θ of any other mode beyond $x/D = 1$ (figure 8*b*). The Strouhal number corresponding to the most amplified waves of all azimuthal orders decreases toward the end of the potential core.

The calculated radial distributions of the amplitudes of the u-component of the oscillations at $0.125 \leqslant x/D \leqslant 4$ are plotted in figure 9 for modes 0 and 1. The axisymmetric mode is depicted by a solid curve and the helical mode by a dotted line. The differences between these modes are becoming more discernible with increasing x/D. For $x/D \leqslant 1$, the differences in the radial distribution of $|u'|$ are small indeed, but the importance of the boundary conditions on the high-speed side of the jet become more pronounced at $x/D \geqslant 2$.

3.2. *The initial evolution of the axisymmetric jet*

The following discussion is concerned with the initial evolution of axisymmetric jets with and without external excitation. In §3.2.1 the limiting case of a thin mixing layer ($R_{\frac{1}{2}}/\theta \gg 1$) is analysed and the results stressing the evolution of different azimuthal modes are compared with some phase-locked data produced by subjecting the jet to axisymmetric and helical excitation. In §3.2.2 the natural (unexcited) initial evolution of the axisymmetric mixing layer is considered.

3.2.1. *The initial evolution of the externally excited jet*

Numerical calculations presented in §3.1.2 (figure 5*a*) suggest that the initial rates of amplification of all azimuthal modes considered are approximately the same, provided $R_{\frac{1}{2}}/\theta \gg 1$. The general implications of these observations may be analysed by defining a small quantity ϵ such that

$$\epsilon \equiv \frac{\theta}{R_{\frac{1}{2}}} \ll 1, \tag{3.7}$$

and rearranging (3.4) to obtain

$$\tilde{F}_p'' + \left[\epsilon(1+\epsilon\tilde{y})^{-1} - \frac{2\tilde{U}_0'}{\tilde{U}_0 - \tilde{c}}\right]\tilde{F}_p' - [m^2\epsilon^2(1+\epsilon\tilde{y})^{-2} + \tilde{\alpha}^2]\,\tilde{F}_p = 0. \tag{3.8}$$

Since $\tilde{y} = O(1)$ within the shear layer (i.e. within the region in which $U' \neq 0$ and $U'' \neq 0$), one may expand the term

$$(1+\epsilon\tilde{y})^{-1} = 1 - \epsilon y + (\epsilon y)^2 - \ldots, \tag{3.9}$$

and this, for $(\epsilon y)^2 < 1$, results in

$$\tilde{F}_p'' - 2\left(\frac{\tilde{U}_0'}{\tilde{U}_0 - \tilde{c}}\right)\tilde{F}_p' - [m^2\epsilon^2 + \tilde{\alpha}^2]\,\tilde{F}_p = -\epsilon\{\tilde{F}_p'(1 - \epsilon y + \epsilon^2 y^2 \ldots) + 2\tilde{F}_p\,\epsilon^2 m^2 y + \ldots\}. \tag{3.10}$$

The terms on the right-hand side of (3.10) are smaller by order ϵ relative to the corresponding terms on the left-hand side and, therefore, can be neglected; hence,

$$\tilde{F}_p'' - 2\left(\frac{\tilde{U}_0'}{\tilde{U}_0 - \tilde{c}}\right)\tilde{F}_p' - [m^2\epsilon^2 + \tilde{\alpha}^2]\,\tilde{F}_p = 0, \tag{3.11}$$

where all the azimuthal information is contained in the square brackets of (3.11), which may be rewritten as follows:

$$m^2\epsilon^2 + \tilde{\alpha}^2 = \theta^2\left[\left(\frac{m}{R_{\frac{1}{2}}}\right)^2 + \alpha^2\right] = \theta^2\left\{\alpha_r^2\left[1 + \left(\frac{m}{\alpha_r R_{\frac{1}{2}}}\right)^2\right] - \alpha_i^2 + 2i\alpha_r\alpha_i\right\}, \tag{3.12}$$

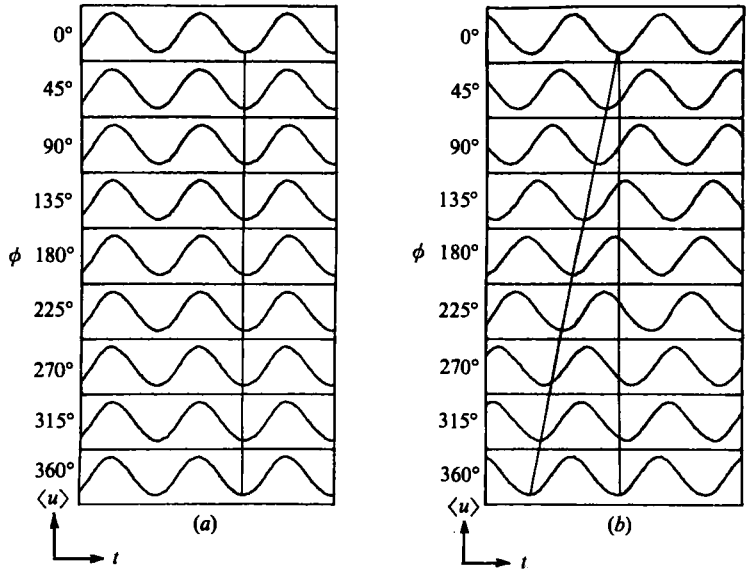

FIGURE 10. Phase-averaged streamwise velocity signatures measured at $x/D = 0.45$, $(r-R_{\frac{1}{2}})/\theta = 0$ and various azimuthal locations while the jet was subjected to a periodic wave having a frequency of 204 Hz and an azimuthal mode number: (*a*) $m = 0$; (*b*) 1.

where the complex eigenvalue α is expressed by its real and imaginary constituents $\alpha = \alpha_r + i\alpha_i$. Since the streamwise wavelength is $\lambda_x = 2\pi/\alpha_r$ and the azimuthal wavelength is $\lambda_\phi = 2\pi R_{\frac{1}{2}}/m$, the term in the square brackets of (3.12) represents the ratio of the two lengths and may be rewritten as

$$\left[1+\left(\frac{\lambda_x}{\lambda_\phi}\right)^2\right].$$

Thus, whenever $(\lambda_x/\lambda_\phi)^2 \ll 1$, (3.11) becomes independent of the azimuthal mode number and is equivalent to the plane Rayleigh equation expressed in terms of pressure fluctuations. Consequently, all azimuthal modes of order unity undergo identical evolution, provided the shear layer emerging from a sizable nozzle is thin (i.e. $\theta/R_{\frac{1}{2}} \ll 1$). The axisymmetric mode $m = 0$ evolves exactly as if the mean flow were two-dimensional; for other modes, the simplification breaks down when the excitation frequency is low (i.e. λ_x is relatively large).

The evolution of the axisymmetric ($m = 0$) and the helical ($m = 1$) modes with downstream distance was investigated experimentally. The exit velocity of the jet was 8.1 m/s with ensuing Reynolds number $Re_D \approx 2.4 \times 10^4$; the excitation frequency (F_f) was 204 Hz, corresponding to a Strouhal number based on the diameter of the nozzle $St_D = F_f D/U_j = 1.28$. Measurements were carried out at nine streamwise locations between $x/D = 0.3$ and 0.7, for which the parameter $R_{\frac{1}{2}}$ satisfies $18 < R_{\frac{1}{2}}/\theta \leqslant 80$, corresponding to a Strouhal-number range based on θ ranging over $0.008 \leqslant F_f\theta/U_j \leqslant 0.035$. The streamwise distance covered in the experiment corresponded approximately to a single wavelength at the excitation frequency.

Typical phase-locked perturbation velocities simultaneously recorded by eight hot wires located at $x/D = 0.45$ and $r = R_{\frac{1}{2}}$ and separated azimuthally by an angle $\phi = \frac{1}{4}\pi$ are shown in figure 10. When the jet was excited by an axisymmetric mode (figure 10*a*), the velocity signals recorded by each sensor at a given time were almost

	Average			Maximum		
x/D	$M=0$	$M=-1$	$M=+1$	$M=0$	$M=-1$	$M=+1$
			(*a*) Excitation of mode 0			
0.30	100.000	5.310	7.939	100.000	6.539	7.006
0.35	100.000	5.708	5.708	100.000	6.593	7.836
0.40	100.000	5.894	8.437	100.000	6.554	8.515
0.45	100.000	6.816	7.886	100.000	6.554	8.535
0.50	100.000	5.598	7.766	100.000	5.958	9.965
0.55	100.000	4.187	7.317	100.000	3.920	8.552
0.60	100.000	4.614	8.062	100.000	4.785	8.564
0.65	100.000	4.301	8.408	100.000	5.557	8.221
0.70	100.000	4.372	8.647	100.000	5.440	9.953
			(*b*) Excitation of mode +1			
0.30	6.668	3.866	100.000	5.366	4.228	100.000
0.35	7.322	3.202	100.000	6.692	2.371	100.000
0.40	7.773	5.465	100.000	6.618	5.723	100.000
0.45	7.755	7.519	100.000	7.045	8.594	100.000
0.50	7.410	7.343	100.000	7.279	9.516	100.000
0.55	8.277	8.039	100.000	9.416	8.307	100.000
0.60	9.031	7.254	100.000	9.194	8.341	100.000
0.65	8.572	9.361	100.000	9.260	12.725	100.000
0.70	8.230	10.531	100.000	8.821	15.322	100.000

TABLE 1. The evolution of azimuthal modes in a jet subjected to external excitation

identical, as shown in the figure. Exciting the jet in a clockwise mode produced a phase delay among the various sensors with a circumferential periodicity of 2π (figure 10*b*). A careful examination of Figure 10 reveals that the velocity signals are not always perfectly sinusoidal and the separation angle ϕ between the two adjacent sensors may not be precisely $\frac{1}{4}\pi$. Nevertheless, the results prove that the jet can be excited by modes that are not axisymmetric.

The relative amplitudes of modes 0, 1 and -1 investigated at the nine streamwise locations are shown in table 1. Two quantities are tabulated for each azimuthal mode number at every x/D considered: (i) the maximum value of the amplitude of a given mode; and (ii) an amplitude that is averaged over all radial locations measured. In both cases, the amplitude of the excited mode was an order of magnitude higher than the amplitudes of the unexcited modes. Thus, over the range of distances considered, the natural coupling among different modes appears to be secondary.

The divergence of the jet, as expressed by the rate of decrease of $R_{\frac{1}{2}}/\theta$ and the rate of growth of θ with x/D, is shown in figure 11. External excitation affects $\mathrm{d}\theta/\mathrm{d}x$ in this flow, as it does in the plane mixing layer (Oster & Wygnanski 1982); it is a nonlinear effect which will be addressed in the future. For $x/D \leqslant 0.45$, the flow is almost parallel and all the measured velocity profiles (figure 12*a*) are self-similar and agree quite well with the profile suggested by Michalke (1971), which is also plotted for comparison. The constancy of θ in this region permits one to plot a single profile to represent the data, in spite of the inherent lack of similarity in the expression suggested by Michalke. Measurements made at larger x/D and plotted in the same coordinates show clearly the absence of similarity and the deviation from the profile

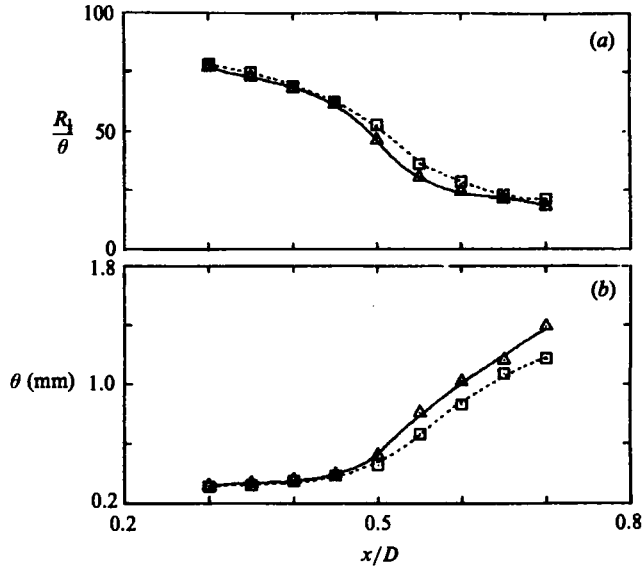

FIGURE 11. The divergence of the jet as expressed by the downstream evolution of (*a*) $R_{\frac{1}{2}}/\theta$, and (*b*) θ, while the jet was subjected to external excitation of a periodic wave having a frequency of 204 Hz and azimuthal mode number: △, $m = 0$; □, 1; $U_j = 8.1$ m/s, $D = 25.4$ mm.

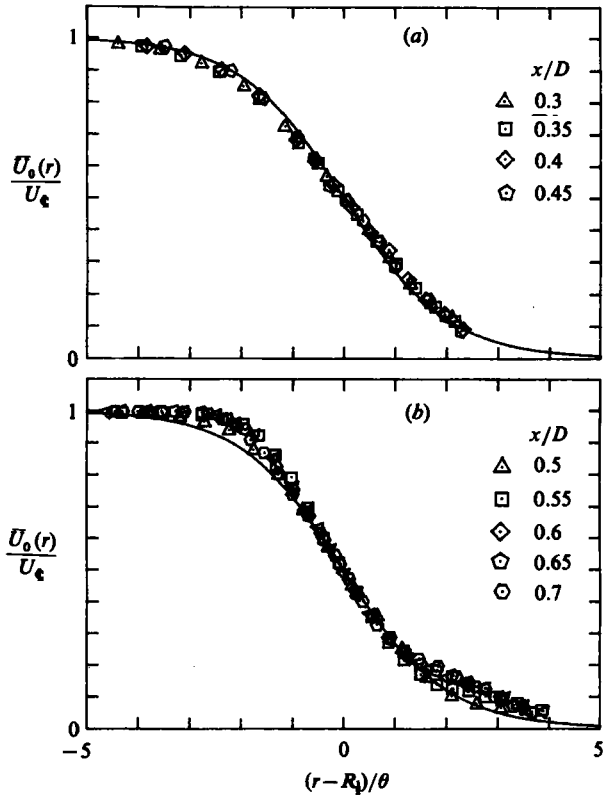

FIGURE 12. Streamwise similarity of mean velocity profiles when the jet was subjected to external excitation with $F_t = 204$ Hz at $U_j = 8{,}1$ m/s, $D = 25.4$ mm and $m = 0$. The solid lines correspond to the analytical expression suggested by Michalke (1971).

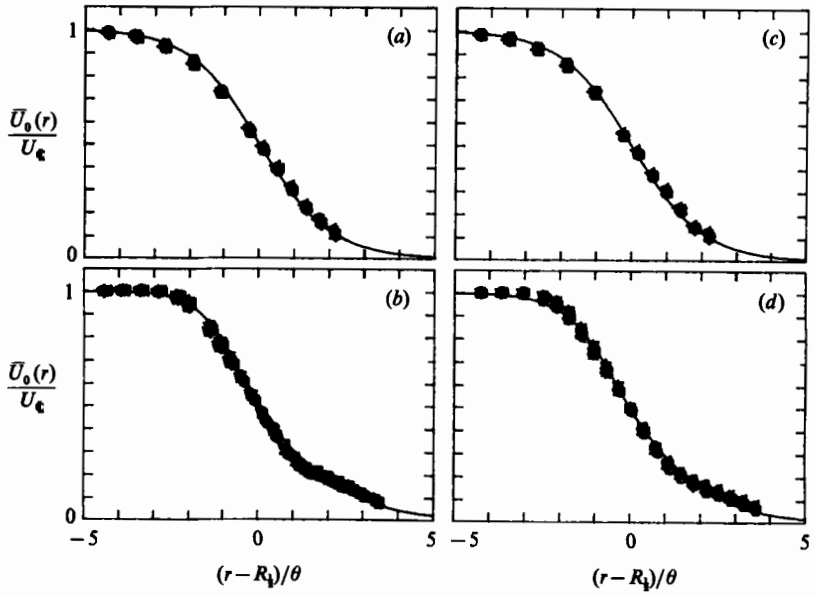

FIGURE 13. Azimuthal similarity of mean velocity profiles for forced jet with forcing frequency 204 Hz, $U_j = 8.1$ m/s, $D = 25.4$ mm. The solid lines are the expression given in equation (3.13). (*a*) $x/D = 0.3$, $m = 0$, $Q = 0$, $w = 0$; (*b*) $x/D = 0.65$, $m = 0$, $Q = 0.2$, $w = 0$; (*c*) $x/D = 0.3$, $m = 1$, $Q = 0$, $w = 0$; (*d*) $x/D = 0.65$, $m = 0$, $Q = 0.125$, $w = 0$.

fitted by Michalke (figure 12*b*). Consequently, for $x/D \geqslant 0.5$, the following analytical expression describing the mean velocity is used in the stability analysis:

$$\frac{\overline{U}_0(r)}{U_j} = 0.5[1+\tanh(\xi)]+Q\tanh^2(\xi)\operatorname{sech}^2(\xi)+W\tanh(\xi)\operatorname{sech}^4(\xi), \quad (3.13)$$

where $\xi = b[R_{\frac{1}{2}}/r - r/R_{\frac{1}{2}}]$ and Q and W are constants representing, respectively, the symmetric and antisymmetric corrections to Michalke's basic profile, which can be recovered by letting $Q = W = 0$. The constant b is related to Q and W by the definition of the momentum thickness, which is determined experimentally and is given by

$$\theta = \frac{R_{\frac{1}{2}}}{b}\left\{\tfrac{1}{4}-\tfrac{2}{15}W-\tfrac{2}{35}Q^2-\tfrac{16}{315}W^2+\tfrac{1}{2}Q\int_{-\infty}^{\infty}[1+2W\operatorname{sech}^4(\xi)]\frac{\tanh^3(\xi)\operatorname{sech}^2(\xi)}{(\xi^2+4b^2)^{\frac{1}{2}}}\xi\,\mathrm{d}\xi\right\}. \quad (3.14)$$

Thus, for given values of Q, W and the momentum thickness, (3.14) can be solved iteratively for b.

The mean profiles, measured at $x/D = 0.3$ and 0.65 while the flow was excited by either mode 0 or mode 1, are plotted in figure 13. The mean flow is axisymmetric for all cases shown in figure 13, as may be deduced from the eight profiles measured at eight different azimuthal locations separated from one another by $\Delta\phi = 45°$. The abscissa in figure 13 is $(r-R_{\frac{1}{2}})/\theta$; the radial position of each probe was adjusted to be zero at $r = R_{\frac{1}{2}}$, while the value of θ used was spatially averaged over the eight azimuthal locations. All the profiles fit the analytical expression given in (3.13) well; this expression is also plotted in figure 13 for each of the four cases considered. For $x/D = 0.3$, Q and W vanish, reducing (3.13) to Michalke's profile, while for $x/D = 0.65$, $Q = 0.2$ for axisymmetric excitation and $Q = 0.125$ for mode 1 excitation.

Calculations of linear stability theory were performed using the mean velocity profile given in (3.13). The radial distributions of the amplitudes of the streamwise velocity fluctuations obtained theoretically for modes 0 and 1 at eight downstream locations are drawn in figure 14 (solid lines). These calculations are compared with experiments by equating the areas under each curve. The experimental results obtained for the axisymmetric excitation are marked by triangular symbols in figure 14, while the results marked by square symbols correspond to the helical mode of excitation. The agreement between the theoretical and the measured radial distributions of amplitudes is fairly good for both modes; in fact, the axial evolution of the first two azimuthal modes is similar, as predicted for the limit $\theta/R_{\frac{1}{2}} \ll 1$.

A critical assessment of the theoretical results associated with the limiting condition of $\theta/R_{\frac{1}{2}} \ll 1$ is done by comparing global quantities integrated across the shear flow, such as the overall amplification rates of the two modes, and then the detailed radial distributions of the amplitudes and the phase angles of the u-fluctuations for both modes of excitation. Three different criteria are used to define the overall amplification rate of the disturbances in the downstream direction: (i) the maximum value of the amplitude of u at each x-station; (ii) the integral of $|u|$ over the area confined between $r = R_{0.95}$ and $R_{0.10}$ corresponding to the radial positions where the mean velocity has the values of 0.95 and 0.1 respectively; and (iii) dividing the integral calculated in (ii) by the area of the flow considered. The gain of $|u|$ is always normalized to unity at the first station x_0 at which measurements were taken. All three methods of assessing the rate of amplification versus $F_{\mathrm{f}}\theta/U_{\mathrm{j}}$ are shown in figure 15. For a given F_{f} and U_{j}, the abscissa in this figure corresponds to a variation in θ (or in x) only. The amplifications of both modes (triangles correspond to $m = 0$ and squares to $m = 1$) are almost identical, irrespective of the criterion used, in the range $R_{\frac{1}{2}}/\theta$ considered (i.e. $R_{\frac{1}{2}}/\theta \geqslant 18$).

The different criteria produce, however, some markedly different results. While the maximum amplitude of u increases initially and saturates smoothly with downstream distance, the integral quantities shown in figure 15(b, c) attain a local maximum at $2\pi F_{\mathrm{f}}\theta/U_{\mathrm{j}} \approx 0.07$, which corresponds to the excitation at which θ starts to increase rapidly with x.

Although the maximum amplitudes of the oscillations, or their area-integrated average, actually decay beyond $St_\theta \geqslant 0.09$ (figure 15a, c), the integral $\int |u| r\,\mathrm{d}r$ increases with St_θ (figure 15b) simply because the width of the shear layer increases. The total energy contained at the excitation frequency may increase with x, in spite of the fact that the local amplitudes may actually decay; this apparent contradiction in terms stems from the divergence of the shear layer.

The radial distributions of the amplitudes and the phases of the u-component of the fluctuations for both modes of excitation are compared at $R_{\frac{1}{2}}/\theta = 71$ and plotted in figure 16. The corresponding theoretical distributions of amplitudes and phases of both modes, which appear to be identical when drawn on the scale of this figure, agree fairly well with experiments.

3.2.2. *The initial evolution of disturbances in the unperturbed jet*

Linear stability theory applied to a parallel shear layer suggests that only the most amplified wave is bound to dominate the flow field some distance downstream (Michalke 1965) because, at the initiation of the flow, the background disturbance may be so broad that it can be legitimately represented as 'white noise'. The exponential amplification of the most unstable wave with downstream distance acts, therefore, as a natural filter. For a velocity distribution described by a hyperbolic

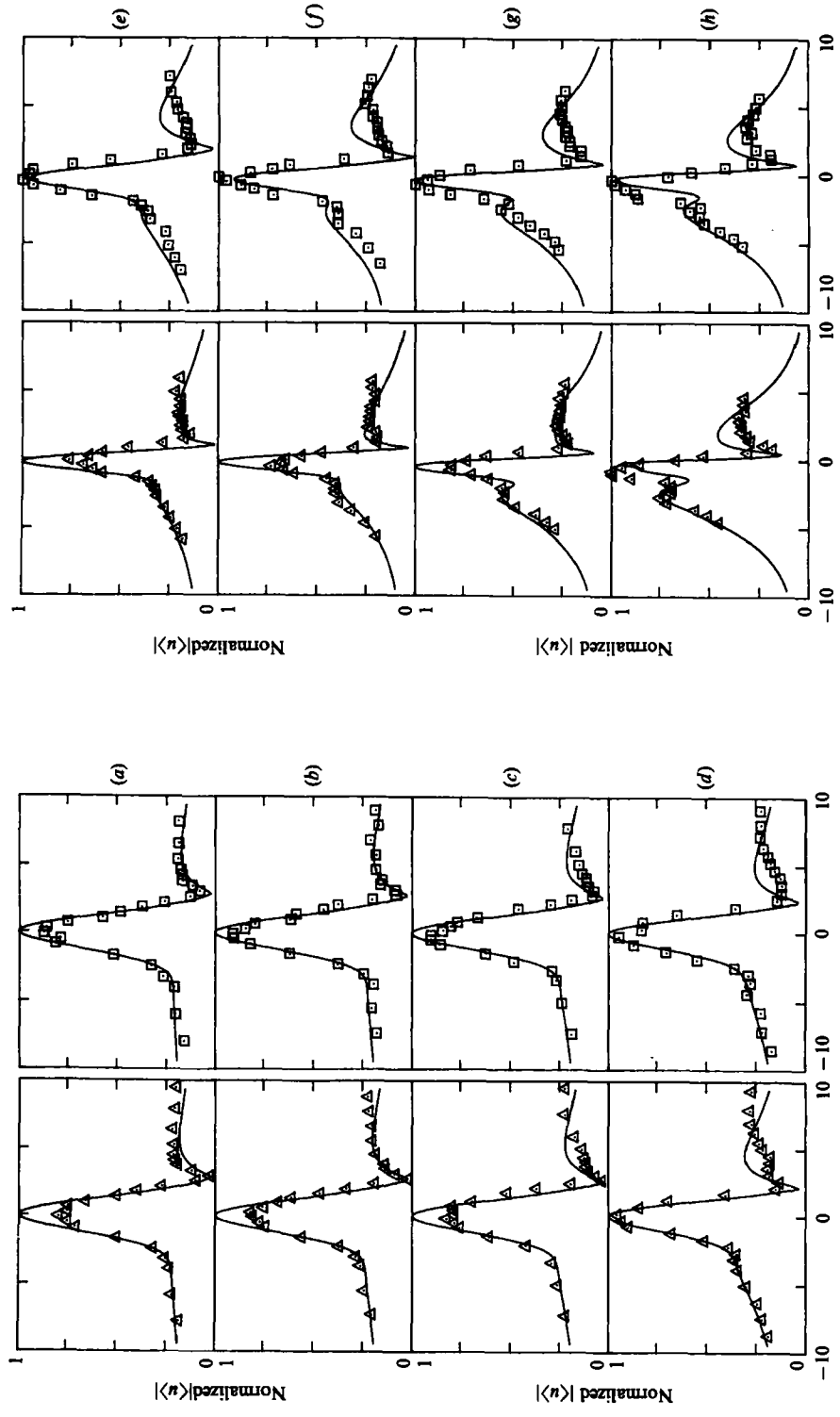

FIGURE 14. Radial distribution of the amplitude of the streamwise velocity fluctuations at several downstream locations: △, $m = 0$; □, $m = 1$; ——, theoretical curves. Data were obtained for $U_1 = 8.1$ m/s. $F_1 = 204$ Hz and $D = 25.4$ mm. (*a*) $x/D = 0.35$, (*b*) 0.40; (*c*) 0.45; (*d*) 0.50; (*e*) 0.55; (*f*) 0.60; (*g*) 0.65; (*h*) 0.70.

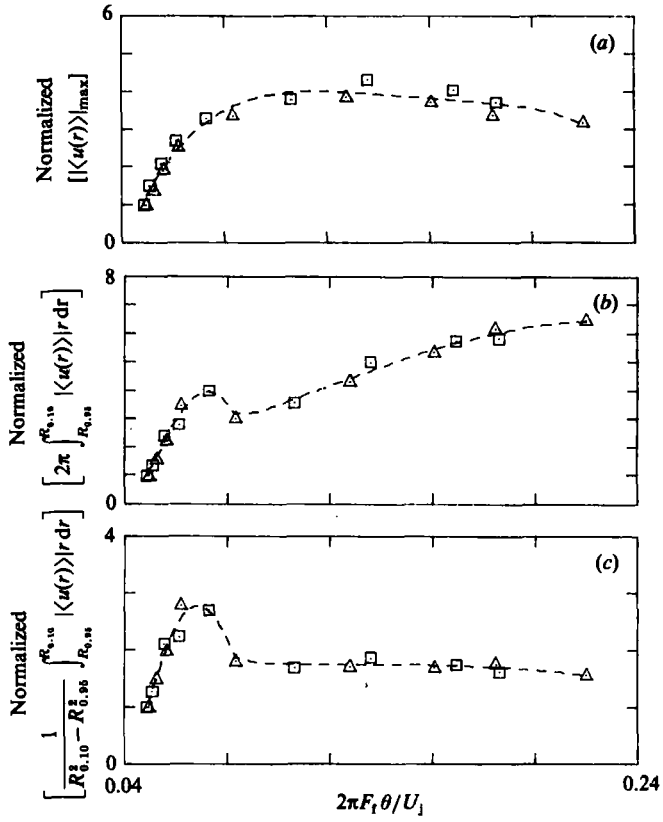

FIGURE 15. Overall normalized amplification rate of the streamwise velocity component of the disturbance as a function of the non-dimensional frequency $2\pi F_f \theta / U_j$: △, $m = 0$; ⊡, 1. The data were obtained for $U_j = 8.1$ m/s, $F_f = 204$ Hz and $D = 25.4$ mm.

tangent of the transverse coordinate, $\tilde{y}$, the Strouhal number St_t corresponding to the most amplified disturbance f_t is equal to $St_t = f_t \theta / U_j = 0.017$, where θ is the initial momentum thickness (which is constant) and U_j is the jet velocity measured in the plane of the nozzle. Measurements reported in the literature (Gutmark & Ho 1983; Husain & Hussain 1979) indicate values over the range $0.009 \leqslant St_t \leqslant 0.018$. Moreover, since most of the jets emerge from smooth and well-designed nozzles, the boundary layers on the inner wall of the contractions are generally laminar and can be represented by the Blasius profile (Drubka 1981). The initial momentum thickness in the plane of the nozzle should therefore vary as $U_j^{-\frac{1}{2}}$. Provided the flow does not spread radially with increasing distance x, the most amplified frequency in the shear layer is given by

$$f_t = 0.017 \frac{U_j}{\theta_t} = C_0 U_j^{\frac{1}{2}}, \tag{3.15}$$

where C_0 is constant. This relationship was verified experimentally by Sato (1956) and by Wehrmann (1960). More recently, however, when fast Fourier transforms replaced analog 'frequency meters', the experiments were repeated at small increments of U_j (Gutmark & Ho 1983), which led to the observation that the prevailing frequency varies in a stepwise manner with increasing U_j rather than following (3.15). This effect may stem either from the facility or from the experimental procedure used.

It was suggested initially that the stepwise behaviour of the predominant

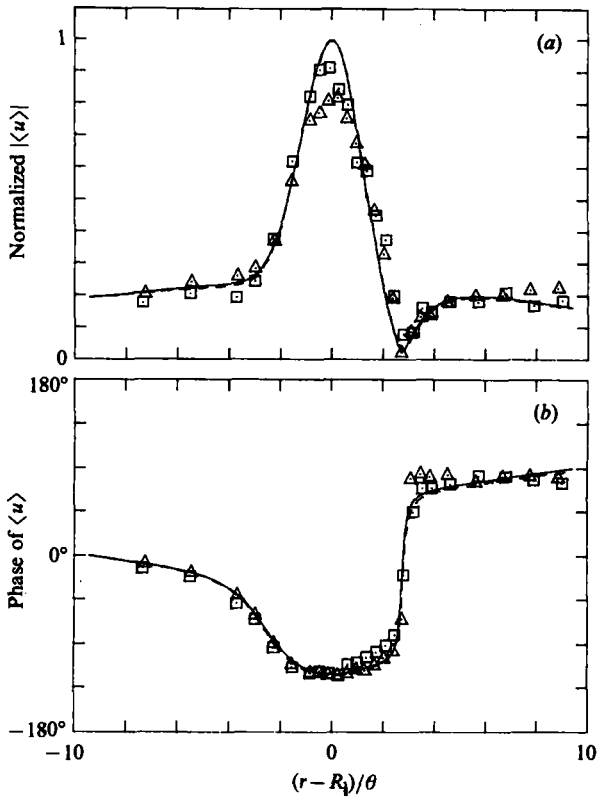

FIGURE 16. The phase-locked (*a*) amplitude and (*b*) phase distributions in the forced jet with forcing frequency 204 Hz, $D = 25.4$ mm and $U_j = 8.1$ m/s measured at $R_i/\theta = 71$. △, $m = 0$; ⊡, $m = 1$; ——, theoretical curve for $m = 0$; – – –, theoretical curve for $m = 1$.

frequency resulted from probe interference (Nagib Hussain, 1980, private communication). Experiments carried out by Einav *et al.* (1981) using, simultaneously and separately, a hot-wire probe and a LDA, which is a non-intrusive instrument, refuted this suggestion entirely. Gutmark & Ho (1983) attributed the stepwise behaviour to an extremely small upstream disturbance detected in a plenum chamber, which produced a spatially coherent disturbance in the plane of the nozzle. Due to the large area ratio between the cross-section of the plenum and the nozzle, any acoustic wave in the plenum will produce a plane wave at the exit of the nozzle, and therefore the initial evolution of disturbances in a jet is expected to be axisymmetric. A coherent wave present in the plenum chamber does not decay along the contraction and nozzle (Blackwelder & Kovasznay 1972) and may excite (in a linear or nonlinear manner) an instability wave in the shear layer. The turbulence level in the centre of most laboratory jets varies between $0.2\,\% \leqslant u'/U_j \leqslant 0.6\,\%$. Such background turbulence is seldom homogeneous, and therefore one may easily expect coherent waves having initial amplitudes larger than 1 % to dominate the flow at the exit plane. Since there is no obvious mechanism dissipating these waves, they may dominate the instability frequency wave over some range of velocities, producing a stepwise variation of the predominant frequency with U_j. This notion is explored and discussed in the following section.

The relationship presented in (3.15) stems from the assumptions that the inviscid

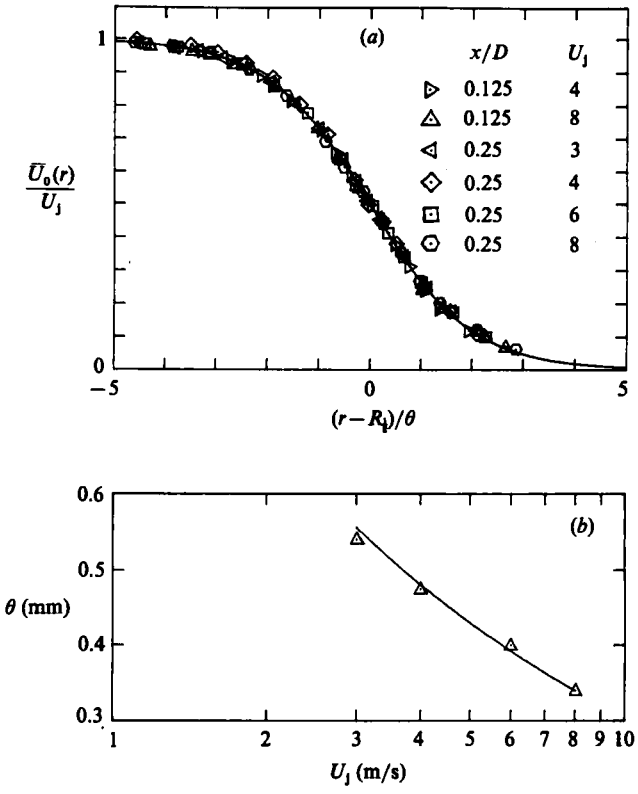

FIGURE 17. (*a*) Mean velocity profiles measured at various downstream locations for several jet exit velocities. The solid line is the analytical expression given by equation (3.16). (*b*) Variation of the momentum thickness with jet exit velocity; △, measurement; ——, a curve representing the relation $\theta \propto U_j^{-\frac{1}{2}}$.

linear stability theory based on a hyperbolic tangent velocity distribution is applicable, and that the initial momentum thickness θ is proportional to $U_j^{-\frac{1}{2}}$. Experiments show (figure 17(*a*)) that the characteristic shape of the velocity profile is retained over $0.125 < x/D < 0.25$ for velocities ranging from 3 to 8 m/s. All the measured profiles fit the equation

$$\frac{\bar{U}_0(r)}{U_j} = 0.5\left[1-\tanh\left(\frac{r-R_{\frac{1}{2}}}{2\theta}\right)\right], \tag{3.16}$$

which is plotted in the same figure (solid line). The variation of the momentum thickness with U_j at $x/D = 0.25$ is shown in figure 17, where the actual data points, marked by triangular symbols, fit the relation $\theta \propto U_j^{-\frac{1}{2}}$ in the range of velocities considered. One therefore expects (3.15) to apply, provided the background disturbance level is uniformly distributed in the spectral domain. Power spectra measured on the axis of the jet in the plane of the nozzle indicate that this is *not* the case, in spite of the fact that the turbulence level varied between 0.1% and 0.17%. Three curves representing power spectra of the streamwise velocity component measured on the centreline of the jet at $x/D = 0$ and corresponding to jet exhaust velocities of 3, 5 and 8 m/s are plotted in figure 18. The spectra were high-pass filtered at 20 Hz and normalized by the highest peak of the spectrum corresponding to $U_j = 3$ m/s. The spectral distributions at all velocities tested are not homogeneous; the peaks in

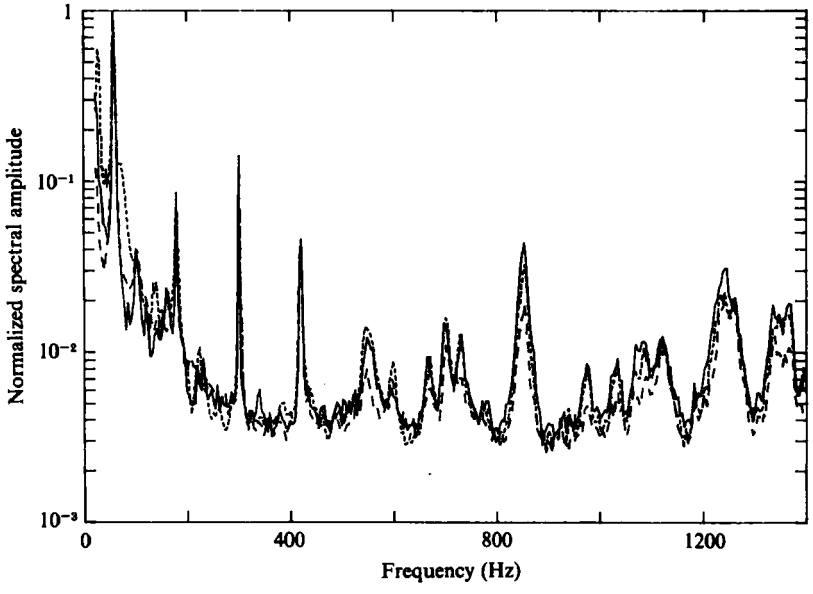

FIGURE 18. Power spectra of the streamwise velocity component measured at $x/D = 0$ and $r/D = 0$. ——, $U_j = 3$ m/s; – – –, 5 m/s; — —, 8 m/s. All the spectral distributions are normalized by this highest peak of the spectrum corresponding to $U_j = 3$ m/s.

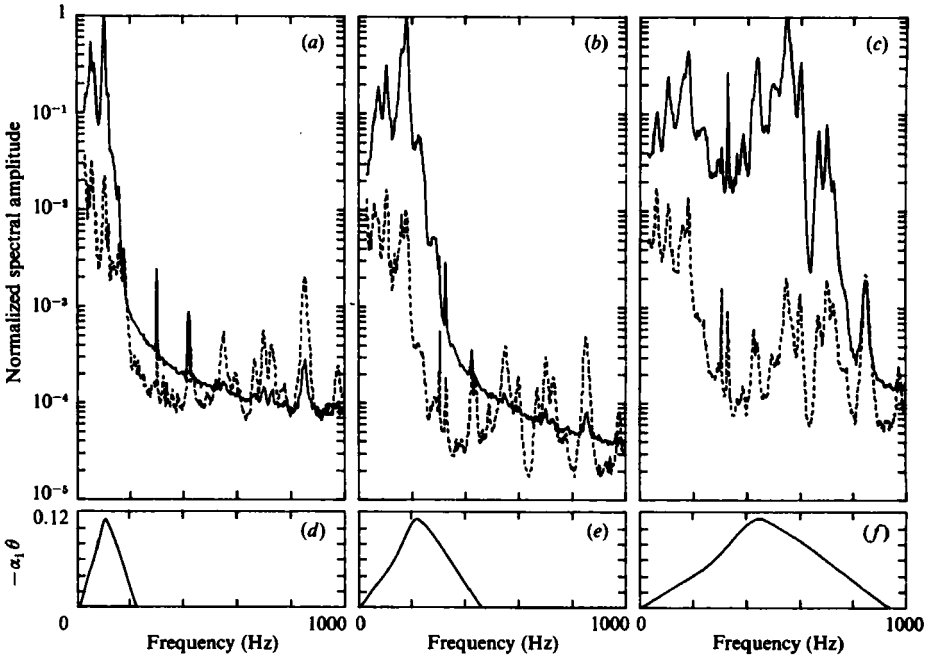

FIGURE 19. Normalized power spectra of the streamwise velocity component as measured for various jet exhaust velocity and corresponding calculated spatial growth rates. The spectral distributions were measured at: ——, $x/D = 0.25, r = R_{\frac{1}{2}}$; – – –, $x/D \approx 0, r = R_{\frac{1}{2}}$. (a, d) $U_j = 3$ m/s; (b, e) 5 m/s; (c, f) 8 m/s.

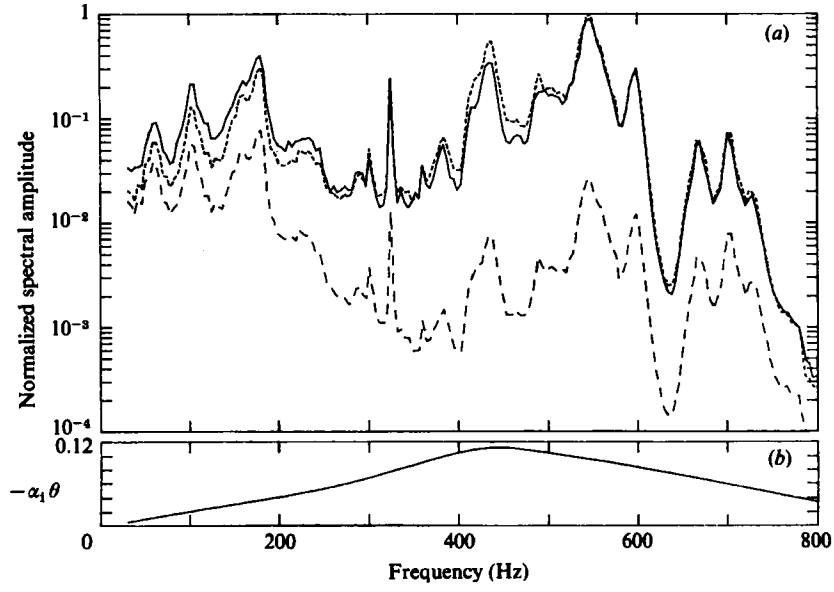

FIGURE 20. (*a*) Power spectra of the streamwise velocity component measured at: ——, $x/D = 0.125$, $r = R_{\frac{1}{2}}$ ——, $x/D = 0.25$, $r = R_{\frac{1}{2}}$ for $U_j = 8.1$ m/s; – – –, predicted spectrum at $x/D = 0.25$ and $r = R_{\frac{1}{2}}$. All spectra are normalized by the highest peak of the predicted spectrum. (*b*) calculated spatial growth rate as a function of the dimensional frequency.

the spectra occur at identical frequencies regardless of the jet velocity (see also Crow & Champagne 1971). Similar peaks in the power spectrum were observed in the centre of the shear layer at $x/D \approx 0$ (i.e. near the tip of the nozzle) as described by the dotted lines in figure 19(*a*, *b*, *c*), corresponding to $U_j = 3$, 5 and 8 m/s respectively. These peaks are broader than their counterparts on the jet centreline, and their relative amplitudes might also differ as a result of the amplification of disturbances in the boundary layer. Using the superposition property, the possible correspondence between the linear stability theory and the observed spectrum farther downstream is first examined qualitatively. The solid lines in figure 19(*a*, *b*, *c*), are the power spectra of the streamwise component of velocity measured at the centre of the shear layer at $x/D = 0.25$ and at $U_j = 3$, 5 and 8 m/s respectively. Each spectrum is normalized by its maximum value, which is also used to normalize the corresponding spectra measured at $x/D = 0$, and represented by dotted lines. The calculated amplification curves for the appropriate $R_{\frac{1}{2}}/\theta$ for each of the velocities chosen are plotted in figure 19(*d*, *e*, *f*) underneath the spectra. For all three velocities, the prevailing frequencies at $x/D = 0.25$ attained a value close to the most unstable frequency f_t, in spite of the fact that the input (i.e. the spectrum at $x/D = 0$) was almost identical for all. However, the exact spectral distribution at $x/D = 0.25$ is strongly dependent on the input. For example, when the most amplified frequency at $U_j = 5$ m/s is in the neighbourhood of 200 Hz ($f_t > 200$ Hz) but a distinct peak in the input spectrum in the vicinity of f_t occurs at a lower frequency, then the exact value of f_t and the prevailing frequency measured may not be the same. Thus, the value of the most energetic frequency observed at any point in the flow is an outcome of both the initial spectral distribution and the amplification curve. One might also notice that the spectra observed at $x/D = 0$ and 0.25 have approximately the same level for frequencies greater than the neutral frequency; in fact, the input spectrum

level might exceed the level of the spectrum measured farther downstream because these waves decay spatially.

Knowing the spectrum at a given x/D, one may attempt to predict the shape of the spectrum farther downstream by using the superposition property of the linear stability model. This type of calculation is quite restricted because it assumes that the mean flow is not altered during the interval and that it does not account for dissipation; nevertheless, it was used for a range of downstream distances ($0.125 < x/D < 0.25$) in which the flow does not diverge and was applied only to the amplified waves.

The broken line in figure 20(*a*) is the spectral distribution of the streamwise velocity component measured at $x/D = 0.125$ and $r = R_{\frac{1}{2}}$ when the jet exhaust velocity was 8.1 m/s; the solid line represents the spectral distribution measured at $x/D = 0.25$ and $r = R_{\frac{1}{2}}$. The amplification shown at the bottom of figure 20 is used as a transfer function applied to the spectrum measured at $x/D = 0.125$ to predict the spectrum at $x/D = 0.25$. The predicted spectrum is represented by the dotted line in figure 20(*a*). Since the maximum value of the predicted spectrum is used to normalize all spectra plotted in figure 20(*a*), the comparison between the predicted spectrum at $x/D = 0.25$ applies to the shape as well as the amplitude.

The agreement between the predicted and measured spectra is fairly good. The most energetic frequency in the input spectrum (180 Hz) decreased at $x/D = 0.25$ because it was not as strongly amplified as the most unstable frequency (430 Hz). The small peak in the spectrum measured at $x/D = 0.125$ at $f = 430$ gained in significance but it did not become as strong as the peak at $f = 550$ Hz, which was amplified at a slower rate than the amplitude corresponding to $f = 430$ and was significantly above the peak in the spectrum occurring at $f = 430$ Hz to begin with.

3.3. *The effects of mean flow divergence*

The mixing layer spreads rapidly when the distance from the nozzle exceeds $x/D > 0.5$ and, consequently, the divergence of the mean flow should be considered. The effects of divergence are of particular interest for $0.5 < x/D < 0.8$, where the ratio $R_{\frac{1}{2}}/\theta$ is still large. Since the mean velocity profiles are not self-similar, as they were in some previous investigations (e.g. Gaster *et al.* 1985), the amount of data that can be used for computational purposes (i.e. for forming derivatives with respect to the streamwise coordinate x) is therefore limited. The data collected at only 9 x-stations located approximately one-eighth of a wavelength apart were to be used for applying the linear stability model to a divergent flow, in comparison with similar calculations (Gaster *et al.* 1985) where 51 or more cross-sections were used. In order to ascertain that these data may suffice for the computations, the results of Plaschko (1979) were first reconstituted using the input describing the mean flow from 9 cross-sections only. The agreement is sufficiently good to inspire confidence whenever these calculations are applied to the current experiment. For this purpose, the results described in figure 15 are replotted using a different scale in figure 21 and are compared with linear stability calculations applied to the slowly divergent mean flow.

The calculated amplification of disturbances with downstream distance exceeds the experimental results by a factor of 2 to 3 (see also Gaster *et al.* 1985; Strange 1981; Strange & Crighton 1983). Surprisingly, however, the predicted amplification of the helical mode exceeds the calculated amplification of the axisymmetric mode (figure 21) in contradiction with the dimensional arguments presented for $R_{\frac{1}{2}}/\theta \gg 1$. The reason for the discrepancy was attributed to the different mean velocities

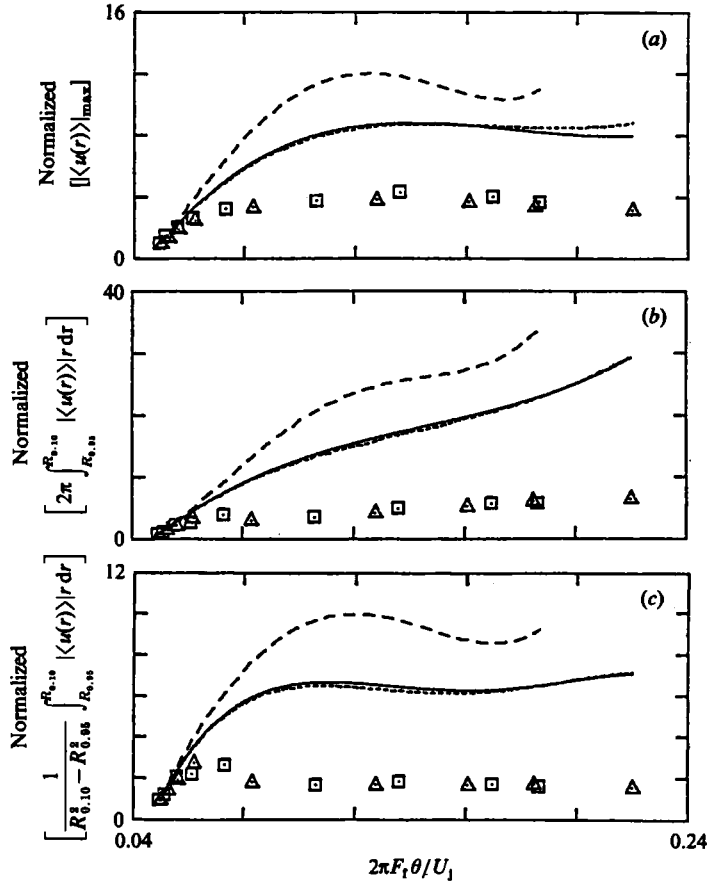

FIGURE 21. Spatial amplification of the excited wave with with $F_f = 204$ Hz and $U_j = 8.1$ m/s. Experimental results: △, $m = 0$; □, 1. Linear stability calculations applied to the slowly divergent mean flow: ——, $m = 0$; — — —, 1; – – –, for $m = 1$ using the mean flow applied to $m = 0$.

encountered in the experiments (see figure 11). This idea was verified by recomputing the amplification rates for mode 1 using the mean velocities applied to mode 0. The results of the calculation for both modes can hardly be distinguished (figure 21). Why then are the mean velocities so different in the same experiment? The differences stem from different excitation amplitudes; the initial amplitude of the axisymmetric mode, being higher, resulted in a more rapid lateral spread of the shear layer (due to a nonlinear interaction) which, in turn, inhibited the amplification of the excited mode. Shifting the virtual origin of the mean flow associated with the helical mode upstream until the data shown in figure 11 collapsed onto a single curve eliminated completely the differences in the rate of amplification of the two modes. This demonstrates the shortcomings of the linear stability theory, which *decouples the initial amplitude of the excitation from rate of spread of the shear layer while, in reality, these effects are not separable.* Because the flow remains parallel for the helical mode for a slightly longer distance (figure 11) than it does for mode 0, it enables mode 1 to amplify by a larger factor (provided $\alpha_i \neq 0$ while the flow was parallel). Therefore, the calculation of total amplification with downstream distance based on the assumption of self-similarity of the mean flows with a known rate of spread ($d\theta/dx$) is not meaningful unless the corresponding absolute value of the initial amplitude is known.

3.4. *Concluding remarks*

One may conclude that the linear stability model predicts correctly the local distribution of amplitudes and phases in an axisymmetric jet excited by external means. The model used as a transfer function is also capable of predicting the entire spectral distribution of velocity perturbations in an unexcited jet over short distances in the direction of streaming. The axisymmetric jet column surrounded by a thin shear layer admits the evolution of an infinite number of helical instabilities in addition to the axisymmetric instability which is independent of the azimuthal coordinate. The possibility that numerous instability modes will coexist and interact among themselves is of special interest since it adds a new degree of complexity to this configuration. The decreasing dimension of the jet column in the direction of streaming selectively filters the higher azimuthal modes, limiting the number of possible nonlinear interactions.

The authors would like to express their appreciation to Drs F. Champagne, M. Gaster, E. Kerschen, A. Newell and R. E. Petersen for the assistance and enlightening discussions. The work was supported in part by the National Science Foundation under grant MEA 8210876 and by NASA under grant NAG 3–460.

REFERENCES

Batchelor, G. K. & Gill, A. 1962 Analysis of the stability of axisymmetric jets. *J. Fluid Mech.* **14**, 529.

Blackwelder, R. F. & Kovasznay, L. S. G. 1972 Large-scale motion of a turbulent boundary layer during relaminarization. *J. Fluid Mech.* **53**, 61.

Bradshaw, P., Ferriss, D. H. & Johnson, S. 1964 Turbulence in the noise producing region of a circular jet. *J. Fluid Mech.* **19**, 591.

Brown, G. L. & Roshko, A. 1971 The effects of density difference on the turbulent mixing layer. In *Turbulent Shear Flows*, AGARD-CP-93, Paper No. 23, pp. 23-1–23-12.

Cohen, J. & Wygnanski, I. 1987 The evolution of instabilities in the axisymmetric jet. Part 2. The flow resulting from the interaction between two waves. *J. Fluid Mech.* **176**, 221.

Crighton, D. G. & Gaster, M. 1976 Stability of slowly divergent jet flow. *J. Fluid Mech.* **77**, 397.

Crow, S. C. & Champagne, F. H. 1971 Orderly structure in jet turbulence. *J. Fluid Mech.* **48**, 547.

Davies, P. O. A. L., Fisher, M. J. & Barratt, M. J. 1963 The characteristics of the turbulence in the mixing region of a round jet. *J. Fluid Mech.* **15**, 337.

Dimotakis, P. E., Lye, R. C. & Papantoniou, D. Z. 1983 Structure and dynamics of round turbulent jets. *Phys. Fluids* **26**, 3185.

Drubka, R. E. 1981 Instabilities in near field of turbulent jets and their dependence on initial conditions and Reynolds number. Ph.D. thesis, Department of Mechanical and Aerospace Engineering, Illinois Institute of Technology, Chicago, USA.

Einav, S., Avidor, J., Gutmark, E. & Gaster, M. 1981 *Bull. Am. Phys. Soc.* **26**, 1251.

Freymuth, P. 1966 On transition in a separated laminar boundary layer. *J. Fluid Mech.* **25**, 683.

Fuchs, H. V. 1972 Space correlations of the fluctuating pressure in subsonic turbulent jets. *J. Sound Vib.* **23**, 77.

Gaster, M., Kit, E. & Wygnanski, I. 1985 Large scale structures in a forced turbulent mixing layer. *J. Fluid Mech.* **150**, 23.

Gutmark, E. & Ho, C. M. 1983 Preferred modes and the spreading rates of jets. *Phys. Fluids* **26**, 2932.

Husain, Z. D. & Hussain, A. K. M. F. 1979 Axisymmetric mixing layer: influence of the initial and boundary conditions. *AIAA J.* **17**, 48.

MATTINGLY, G. E. & CHANG, C. C. 1974 Unstable waves on an axisymmetric jet column. *J. Fluid Mech.* **65**, 541.

MICHALKE, A. 1965 On spatially growing disturbances in an inviscid shear layer. *J. Fluid Mech.* **23**, 521.

MICHALKE, A. 1971 Instabilität eines Kompressiblen Runden Freistrahls unter Berücksichtigung des Einflusses der Strahlgrenzschichtdicke, *Z. Flugwiss.* **9**, 319.

MICHALKE, A. & HERMANN, G. 1982 On the inviscid instability of a circular jet with external flow. *J. Fluid Mech.* **114**, 343.

OSTER, D. & WYGNANSKI, I. 1982 The forced mixing layer between parallel streams. *J. Fluid Mech.* **123**, 91.

PETERSEN, R. A. 1978 Influence of wave dispersion on vortex pairing in a jet. *J. Fluid Mech.* **89**, 469.

PLASCHKO, P. 1979 Helical instabilities of slowly divergent jets. *J. Fluid Mech.* **92**, 209.

SATO, H. 1956 Experimental investigation on the transition of a laminar separated layer. *J. Phys. Soc. Japan*, **11**, 702.

STRANGE, P. J. R. 1981 Spinning modes in orderly jet structure and jet noise. Ph.D. thesis, Dept. of Applied Mathematical Studies, University of Leeds, UK.

STRANGE, P. J. R. & CRIGHTON, D. G. 1983 Spinning modes on axisymmetric jets. *J. Fluid Mech.* **134**, 231.

WEHRMANN, O. 1960 Characteristics of Separated Cylindrical Boundary Layers. DVL-Bericht, No. 131.